Sulfur Encapsulation by MOF-Derived CoS2 Embedded in Carbon Hosts for High-Performance Li–S Batteries

Journal:	*Journal of Materials Chemistry A*
Manuscript ID	TA-ART-06-2019-006947.R1
Article Type:	Paper
Date Submitted by the Author:	16-Aug-2019
Complete List of Authors:	Zhang, Na; Cornell University, Yang, Yao; Cornell University, Chemistry & Chem Bio Feng, Xinran; Cornell University, Chemistry Yu, Seung-Ho; Korea University, Department of Chemical and Biological Engineering Seok, Jeesoo; Cornell University, Chemistry Muller, David; Cornell University, School of Applied and Engineering Physics Abruna, Hector; Cornell University, Chemistry & Chem. Bio.

SCHOLARONE™
Manuscripts

Sulfur Encapsulation by MOF-Derived CoS$_2$ Embedded in Carbon Hosts for High-Performance Li–S Batteries

Na Zhang,[†, #] Yao Yang,[†, #] Xinran Feng,[†, §] Seung-Ho Yu,[†, ⊥]Jeesoo Seok,[†]

David A. Muller,[‡, △] and Héctor D. Abruña[†, *]

[†] Baker Laboratory, Department of Chemistry and Chemical Biology, Cornell University, Ithaca, New York, 14853, United States

[‡] School of Applied and Engineering Physics, Cornell University, Ithaca, New York 14853, United States

[§] Cornell High Energy Synchrotron Source (CHESS), Cornell University, Ithaca, New York 14850, United States

[△] Kavli Institute for Nanoscale Science, Cornell University, Ithaca, New York 14853, United States

[⊥]Department of Chemical and Biological Engineering, Korea University, 145 Anam-ro, Seongbuk-gu, Seoul 02841, Republic of Korea

Abstract

Li–S batteries have attracted great attention for their combined advantages of potentially high energy density and low cost. To tackle the capacity fade from polysulfide dissolution, we have developed a confinement approach by *in situ* encapsulating sulfur with a MOF-derived CoS$_2$ in a carbon framework (S/Z-CoS$_2$), which in turn was derived from a sulfur/ZIF-67 composite (S/ZIF-67) via heat treatment. The formation of CoS$_2$ was confirmed by X-ray absorption spectroscopy (XAS) and its microstructure and chemical composition were examined through cryogenic scanning/transmission electron microscopy (Cryo-S/TEM) imaging with energy dispersive spectroscopy (EDX). Quantitative EDX suggests that sulfur resides inside the cages, rather than externally. S/hollow ZIF-67-derived CoS$_2$ (S/H-CoS$_2$) was rationally designed to serve as a control material to explore the efficiency of such hollow structures. Cryo-STEM-EDX mapping indicates that the majority of sulfur in S/H-CoS$_2$ stays outside of the host, despite its high void volumetric

fraction of ~85%. The S/Z-CoS$_2$ composite exhibited highly improved battery performance, when compared to both S/ZIF-67 and S/H-CoS$_2$, due to both the efficient physical confinement of sulfur inside the host and strong chemical interactions between CoS$_2$ and sulfur/polysulfides. Electrochemical kinetics investigations revealed that the CoS$_2$ could serve as an electrocatalyst to accelerate the redox reactions. The composite could provide an areal capacity of 2.2 mAh/cm^2 after 150 cycles at 0.2C and 1.5 mAh/cm^2 at 1C. This novel material provides valuable insights for further development of high-energy, high-rate and long-life Li–S batteries.

Introduction

Lithium–sulfur (Li–S) batteries have been considered as one of the most promising next-generation electrical energy storage systems due to their ultrahigh theoretical capacity (1675 mA h g^{-1}), low cost and environmental friendliness of sulfur.[1-4] However, the large-scale application/deployment of Li–S batteries is still impeded by multiple challenges. First, the insulating nature of sulfur and its discharge products, Li$_2$S$_2$/Li$_2$S, gives rise to a limited utilization of the active material, especially at high C-rates. More importantly, high-order lithium polysulfides (Li$_2$S$_x$, $4 \leq x \leq 8$), present as intermediate products during cycling, have a high solubility in the liquid electrolyte, so that they can shuttle between the two electrodes, reacting at both sides, and inevitably leading to fast capacity fade and decreased coulombic efficiency.[5-8] Once the soluble and highly polar lithium polysulfides (LiPSs) are formed, they can easily lose electrical contact with the conductive matrix, due to their poor affinity, increasing the charge transfer resistance and slowing the kinetics of the polysulfides redox reactions.[9] In addition, the large volumetric change (80%) of sulfur during discharge can also affect the integrity of the electrodes.[10] Inspired by the pioneering work of Nazar *et al.*[11] using mesoporous carbon CMK-3 to encapsulate sulfur, carbonaceous materials with various morphologies as sulfur hosts, have been reported to improve the electronic conductivity of the sulfur electrode and mitigate the diffusion of LiPSs. These carbonaceous materials, for example, porous carbons,[12-14] nanotubes,[15-17] graphene/graphene oxides,[18-21] and polymers,[22-23] can enhance the performance of sulfur electrodes by physical constraint/confinement. However, when considering long-term cycling and rate performance, it is difficult for a carbon host, by itself, to meet all the above-mentioned requirements. It is likely that since carbon is nonpolar in nature, it cannot provide efficient trapping of highly-polar and ionic polysulfides.[24]

Recently, polar materials, including metal oxides and metal sulfides, have been investigated as sulfur hosts and employed in composites with sulfur in Li–S cells. Polar hosts, such as metal oxides,[25-29] metal sulfides,[30-35] metal nitrides[36-37] and MXenes[38-42] have been found to adsorb LiPSs by strong chemical binding, and/or by forming intermediate complexes. However, most of these polar hosts are non-conducting materials and thus cannot transport electrons effectively.[24, 29] In addition, the limited surface area of these hosts cannot provide sufficient contact area for chemical interactions with LiPSs, or physically entrap lithium sulfides within the hosts. In the synthesis of sulfur containing composites, melt-diffusion is a popular and routine method to infuse sulfur into the pores of the hosts. However, recent work by the Liu group[43] has shown that melting sulfur into the host materials poses some problems. For example, the sulfur species formed by melt diffusion are often in the form of a continuous film, which leads to the preferential deposition of Li_2S on it. This forms a passivating layer that blocks charge transfer, severely affecting capacity, cycle life and rate performance. Fabricating sulfur composites by *in situ* encapsulating sulfur within a conductive hybrid framework that combines both physical entrapment and chemical interactions, can serve as a promising method to synergistically enhance utilization of the active material and mitigate shuttling issues.

Metal-organic-framework (MOF) materials have been studied as sulfur host materials, due to their facile and cost-effective synthesis, high surface area and tunable porosity. In addition, both the open metal centers and heteroatomic dopant sites can show strong adsorption ability towards lithium polysulfides.[10, 44-49] Zeolitic imidazolate framework-67 (ZIF-67), which is composed of metal ions (Co^{2+}) and an organic compound (2-methylimidazole) is a popular type of MOF.[50] Most previous work utilizing MOF in Li–S cells is based on melt diffusing sulfur into the pores of the MOF materials or initially carbonizing the MOF and subsequently infusing sulfur into the pores via melt diffusion.[44, 51-55] Much less work has been conducted by *in situ* encapsulating sulfur by ZIF materials. It should be noted that ZIFs, in themselves, are not conducting due to the existence of organic linkers,[10] so that compositing (insulating) sulfur with a non-conductive ZIF will slow down the charge transfer kinetics of adsorbed polysulfides, leading to a low utilization of active material as well as poor cycling and rate performance.

We have developed a procedure for the *in situ* encapsulation of sulfur nanoparticles by ZIF-67, followed by heat treatment, in vacuum, to carbonize the MOF (rendering it conductive) so as to enhance the conductivity of the composite. More importantly, we found that after the heat

treatment, the ZIF-67 was converted, by sulfur, to CoS_2 within the carbon matrix. This CoS_2 in the carbon framework served as a conductive host to help encapsulate sulfur into its interior structure. Moreover, it has been reported that cobalt pyrite, CoS_2, is a sulfiphilic semi-metallic material that could effectively adsorb LiPSs, by chemical interactions, and, furthermore, could also serve as an electrocatalyst to boost Li–S battery performance by enhancing the redox reactions of polysulfides.[56] Thus, the resulting composite material, sulfur encapsulated by CoS_2 embedded in a conducting carbon matrix derived from ZIF-67 (S/Z-CoS_2), would synergistically benefit from their combined properties. First, the conductive host, CoS_2 embedded in the carbon matrix, can facilitate electron transfer and ionic transport, increasing the utilization of active material during cycling and enhancing rate performance. Secondly, due to the *in situ* encapsulation, LiPSs diffusion can be largely suppressed by physical entrapment. Thirdly, CoS_2 can serve as both an adsorbent and electrocatalyst for LiPSs. Polar CoS_2 can adsorb polysulfides by chemical interactions and, more importantly, promote the kinetics of the redox reactions. In addition, the materials were obtained by a facile synthesis procedure amenable to large-scale production. With these advantages, the S/Z-CoS_2 composite could deliver, in Li–S cells, a high areal capacity of 2.2 mAh cm^{-2} for over 150 cycles at 0.2 C and excellent cycle performance at both low and high current densities. An outstanding rate performance was also achieved at 5.0 C. S/Z-CoS_2 electrodes with stable and high-areal capacity represent attractive and feasible high energy-density materials for commercial implementation of Li–S batteries.

Experimental section

Preparation of S/ZIF-67

Sulfur nanoparticles were synthesized according to our previous report.[22] In a typical synthesis procedure, 0.015 mol of $Na_2S_2O_3$ dissolved in 50 mL of water were added to 500 mL of a 30 mM sulfuric acid solution containing 1 wt.% of polyvinylpyrrolidone (PVP, Mw ~40,000). After reacting for 2 hours, the resulting sulfur nanoparticles were separated by centrifugation. The obtained particles were homogeneously dispersed in 50 mL of methanol with 2 wt.% PVP. 1.95 mmol of $Co(NO_3)_2 \cdot 6H_2O$ were dissolved in the sulfur/PVP methanol dispersion and the mixture was stirred for 30 min. 5.85 mmol of 2-methylimidazole were added to 50 mL of methanol and after uniformly mixing, the 2-methylimidazole solution was quickly poured into the sulfur mixture. After stirring for 5 min, the mixture was aged for 24 hours at room temperature.

Preparation of S/Z-CoS$_2$

S/Z-CoS$_2$ was synthesized by heat treatment under vacuum. The as-prepared S/ZIF-67 composite was sealed in a quartz tube under vacuum, followed by heating at 300 ºC for 7 h.

Preparation of hollow ZIF-67

To obtain solid ZIF-67, 1.95 mmol of Co(NO$_3$)$_2$ · 6H$_2$O and 5.85 mmol of 2-methylimidazole were dissolved in 50 mL of methanol. After fully dissolving, the 2-methylimidazole solution was quickly added into the former solution and after stirring for 5 min, the mixture was aged for 24 hours at room temperature.[57-58] Tannic acid has been reported to be able to etch the solid MOF to form hollow materials.[59] Thus, the solid ZIF-67 was further treated with tannic acid through a modified method. Typically, 50 mg of solid ZIF-67 particles were dispersed in 50 mL of methanol containing 500 mg of tannic acid. After reaction for 1 hour, the particles were collected by centrifugation.

Preparation of S/H-CoS$_2$

Sublimed sulfur, and as-prepared hollow ZIF-67 were mixed in a mortar and then sealed under vacuum. After heat treatment at 300 ºC for 7 hours, S/H-CoS$_2$ was obtained.

Preparation of Li$_2$S$_6$

A Li$_2$S$_6$ solution was prepared by dissolving stoichiometric amounts of Li$_2$S and elemental S into 1,2-dimethoxyethane and 1,3-dioxolane (DME/DOL, 1:1 in volume) at 60 ºC overnight in an argon glovebox.

Material characterizations

X-ray characterization:

Co K-edge X-ray absorption spectroscopy (XAS) measurements were conducted at the F-3 beamline of the Cornell High Energy Synchrotron Source (CHESS) in transmission mode from 150 eV below the metal edge out to k=12 using nitrogen-filled ion chambers. A Co metal foil spectrum was collected concurrently, and served as a standard to calibrate the incident X-ray energy. XANES (X-ray absorption near edge structure) and EXAFS (extended X-ray absorption fine structure) spectra were normalized and analyzed using the DEMETER (Athena and Artemis) software package.[60] Background removal and spectral normalization were carried out using Athena, and EXAFS fitting was performed with the Artemis package using standard procedures. Fourier transformed EXAFS spectra were obtained by applying a Hanning window from 3 to 10 Å^{-1} with k^2-weighting. Spectra of S/ZIF-67 and S/Z-CoS$_2$ were fitted with standard ZIF-67 and

CoS$_2$ crystal structures, respectively. X-ray diffraction (XRD) patterns were recorded using a Rigaku Ultima VI diffractometer with a Cu Kα source. Diffraction patterns were collected at a scan rate of 5 ° min^{-1} and with an increment of 0.02 °.

Cryogenic electron microscopy characterization:

Sulfur-containing samples were dispersed in ethanol and transferred to Cu TEM transmission electron microscope (TEM) grids with a lacey carbon film (Electron Microscopy Sciences, EMS). The TEM grids were loaded into a Gatan model 914 single-tilt cryo-holder under nitrogen gas, at near liquid N$_2$ temperature. The holder kept the sample at a stable temperature of about -183 ºC to suppress sulfur sublimation. Cryogenic Bright-field (BF) TEM and High-angle annular dark-field (HAADF) STEM images were acquired using a field-emission-gun (FEG) FEI Tecnai F-20 microscope. XEDS elemental mapping was performed using an Oxford X-Max detector. EDX maps were acquired for 10-15 min to achieve more than 100 counts/pixel for sulfur and more than 50 counts/pixel for cobalt before noticeable sample drift was observed. STEM-EDX mapping was set at a beam voltage of 200 keV, a beam dose of 6-7 e/(nm^2 · s) and a pixel size of 128 × 128. Beam damage of STEM-EDX maps has been routinely examined before and after EDX mapping. For Cryo-SEM imaging, sulfur-containing samples were loaded onto a single-crystal Si wafer on a cryo-SEM stage at -165 ºC with a surrounding cold finger set at -183 ºC to prevent ice contamination. Samples were imaged using a FEI Strata 400 STEM FIB electron microscope with a beam voltage of 30 keV and beam current of 1 nA.

Electrochemical tests

The cells were assembled with the prepared sulfur composite electrodes (composite: Super P : PVDF = 80 : 15 : 5 by weight), lithium foil, electrolyte and separator (Celgard 2300) in an argon filled glovebox with low H$_2$O and O$_2$ levels (<0.3 ppm). The electrolyte was 1.0 M lithium bis(trifluoromethane) sulfonamide (LiTFSI) dissolved in a mixed solvent of 1,3-dioxolane (DOL) and 1,2-dimethoxyethane (DME) (1:1, v/v) with 0.2 M LiNO$_3$ as an additive. The galvanostatic charge/discharge and cyclic voltammetry (CV) tests were performed on an Arbin battery cycler (Arbin, BT 2000, USA) between 1.7 to 3.0 V (vs. Li$^+$/Li). The specific capacity and C rates (1C = 1675 mA g^{-1}) were calculated based on the sulfur mass in the electrode.

Results and discussion

Materials synthesis and characterization The S, composited with CoS$_2$ in the carbon matrix derived from ZIF-67 (S/Z-CoS$_2$), was synthesized as illustrated in Figure 1. Sulfur nanoparticles

(NPs) were prepared via the method we previously reported.[22] The sulfur NPs were *in situ* encapsulated by ZIF-67 in the presence of polyvinylpyrrolidone (PVP). To increase the conductivity of the composite, the obtained S/ZIF-67 composite was annealed under vacuum to carbonize the ZIF-67. Figure S1 shows that the purple S/ZIF-67 changed to black after heat treatment. X-ray diffraction (XRD) patterns (Figure 2a) indicate that the S/ZIF-67 composite is a mixture of ZIF-67 and sulfur. After the heat treatment, cubic-phase CoS_2 (JCPDS No. 41-1471) formed. Distinct diffraction peaks at 27.8, 32.5, 36.2, 39.5, 46.5 and 55.2 ° can be indexed to the (111), (200), (210), (211), (220) and (311) crystal planes of CoS_2, respectively. The broad peaks of CoS_2 indicate a small crystal (domain) size and, based on the Scherrer equation, the average size of the crystallites was calculated to be 20~25 nm.

In order to further confirm the formation of CoS_2 in the S/ZIF-67 derived composite after heat treatment, we performed powder X-ray absorption spectroscopy (XAS) measurements at the Cornell High Energy Synchrotron (CHESS). The extended X-ray absorption fine structure (EXAFS) spectra exhibited a significant change between S/ZIF-67 and S/Z-CoS_2 (Figure 2b). The first shell peak, representing the chemical bond between Co and its closest neighbors, at around 1.5 Å in the S/ZIF-67 sample shifted to about 1.9 Å in S/Z-CoS_2 (both without phase correction), suggesting a transformation from a Co-N bond in ZIF-67 to a Co-S bond in CoS_2. The Co-N and Co-S bond lengths were calculated to be 1.988 Å and 2.253 Å, respectively, through EXAFS fitting using ZIF-67 and CoS_2 standards, respectively (Figure S2). Powder X-ray absorption near edge structure (XANES) spectra at the Co-K edge further confirmed that the majority of Co in ZIF-67 was successfully converted to CoS_2, as evidenced by the shift in the Co K-edge energy, as well as the similar spectral features between S/Z-CoS_2 and the CoS_2 standard (Figure S3). Moreover, the signature pre-edge peak feature for S/ZIF-67 disappeared after heat treatment, indicating a decomposition of the MOF structure. In addition, the microstructure of the S/Z-CoS_2 composite particles was examined by bright-field (BF) TEM under cryogenic conditions. As shown in Figure 2c, S/Z-CoS_2 exhibits a projected hexagonal symmetry with a rough surface morphology. The atomic-scale BF-TEM image in Figure 2d reveals a lattice d-spacing of 2.3 Å, which matches the (211) lattice plane of CoS_2. Raman spectra of the composites before and after the heat treatment were presented in Figure S4a. Two new dominant peaks were found at 1350 cm^{-1} and 1585 cm^{-1} corresponding to the characteristic D and G bands of the carbon matrix, respectively, demonstrating that ZIF-67 was carbonized during the heat treatment. About 78 wt.% of elemental

sulfur was incorporated in the S/ZIF-67, while it was 59 wt.% in the S/Z-CoS$_2$ as determined from thermogravimetric analysis (TGA) in Figure S4b.

Traditionally, researchers have employed scanning/transmission electron microscopy (SEM/TEM) to study the microscale and nanoscale distribution of sulfur in host materials. However, under the high-vacuum conditions (10^{-5} Pa) of conventional electron microscopes, elemental sulfur readily sublimes, and some of the sublimed sulfur can redistribute to other parts of the sample, precluding the intrinsic distribution of sulfur from being reliably characterized.[61-65] Our previous work has shown that cryogenic scanning/transmission electron microscopy (cryo-S/TEM) can effectively suppress sulfur sublimation by keeping the sample at near liquid N$_2$ temperature, enabling a reliable characterization of the distribution of sulfur in sulfur-host material composites.[66-68]

The cryo-SEM image of the S/ZIF-67 composite displays a 2-3 μm particle with the typical geometry of a rhombic dodecahedron with twelve rhombic faces (Figure 3a and Figure S5a). The 2D projected geometry of a rhombic dodecahedron can be either a hexagon or rhombus. Cryo-STEM image of S/ZIF-67 composite at T = -183 ºC shows a particle with a hexagonal symmetry and well-defined sharp edges (Figure 3b). The corresponding EDX elemental maps in Figures 3c-e demonstrate the homogenous distribution of Co and S elements in the composite particle at the nanometer scale, which is supported by further examination of the elemental distribution of Co and S in four other different regions (Figure S6). The signals in S and Co maps reached more than 100 and 50 counts/pixel, respectively, before noticeable sample drift and beam damage was observed (Figure S7). Considering that the signal-to-noise (S/N) ratio is proportional to $\sqrt{N}$, S and Co elemental maps have a high S/N ratio of more than 10 and 7, respectively. This confirms the successful encapsulation of sulfur in the ZIF-67 cage. In contrast to the well-defined sharp edges in Figures 3a-b, S/Z-CoS$_2$, obtained by heat treatment, exhibits a rougher surface morphology as shown in the cryo-SEM image in Figure 3f and Figure S5b, as was previously confirmed by BF-TEM images (Figure 2d) to have CoS$_2$ nanoparticles on the surface. The Cryo-STEM image of a S/Z-CoS$_2$ particle reveals a size of 2-3 μm with hexagonal symmetry, similar to S/ZIF-67 (Figure 3g). The corresponding EDX elemental maps of Co, S and Co vs. S again demonstrate the homogenous elemental distribution of Co and S in the S/Z-CoS$_2$ composite, which is further evidenced by the EDX maps of other different S/Z-CoS$_2$ composite particles (Figure S8). To quantitatively examine the S and Co content in the S/Z-CoS$_2$ composite, EDX spectral analysis

was performed and the S to Co atomic ratio was calculated to be 6.7:1 based on the S and Co K-edges peak intensity ratio (the S/Co ratio of CoS_2 is 2:1) (Figure S9), indicating that a significant amount of elemental sulfur stays inside the CoS_2 cages after the heat treatment. This is critical and unique to our design, differing from the conventional strategy in which sulfur stays outside the host material, such as the ones in our previous studies of a porous metal oxide,[29] porous carbon,[67] and layered metal sulfide.[68] The homogenous encapsulation of sulfur in the matrix formed by CoS_2 and carbon can facilitate both electronic transport and the electrochemical utilization efficiency of the insulating sulfur.

The S/Z-CoS_2 composite was obtained by the unique strategy of enclosing sulfur into the ZIF-derived CoS_2 in the carbon framework. A common approach in the literature, to constrain elemental sulfur with a hollow[37,69] or porous host material,[29,51,55,70-71] is through a traditional sulfur melt-infusion method at 155 °C or sulfur vaporization at higher temperatures. Thus, in order to compare our method with the traditional strategy, a control group of hollow ZIF-67 was prepared (see Figure 1 for an illustration of the detailed preparation). In this case, hollow ZIF-67 was obtained by etching solid ZIF-67 using tannic acid (see Figure S1 for the color of hollow ZIF-67).[59] Subsequently, sulfur was infiltrated into the hollow structure under the same heat treatment used so that ZIF-67 was transformed to CoS_2 embedded in a carbon matrix, and sulfur would sublime and infiltrate into the hollow host material at the same time. The formed composite is denoted as S/H-CoS_2. Since the image intensity in ADF-STEM images is proportional to atomic number as well as atomic density, a lower intensity indicates a lower atomic density in the material with the same element. Based on this argument, Figures 4a-4b suggest that the hollowed architecture was successfully obtained and μm-sized ZIF-67 precursors generated an inner void with a shell thickness of about 100 nm. A hollow ZIF-67 particle with a size of 2 μm and a shell thickness of 100 nm will result in a high theoretical void volume fraction of around 85% in the whole particle based on the geometry of a rhombic dodecahedron (Volume, $V = \frac{16\sqrt{3}}{9}a^3$, where a is the edge length).

The microstructure and chemical composition of S/H-CoS_2 composites were examined through Cryo-STEM-EDX mapping. EDX elemental maps of S/H-CoS_2 provide insights as to the local distribution of sulfur, both within as well as outside the hollow host (see STEM images in Figures 4c-f). Analysis of the EDX spectrum, extracted from one particle in the white dashed box in Figure. 4f, suggests a S/Co atomic ratio of 9.5:1, which is larger than the theoretical S/Co ratio of 2:1 in

CoS$_2$ (Figure S10). This indicates that a large amount of (likely) elemental sulfur stays within the region of the hollow ZIF-67 derived host. More importantly, an isolated μm-sized particle in bright green in Figure 4f was ascribed to be a pure elemental sulfur particle outside of the Co-containing hollow host. This would suggest that sulfur coexists both in the elemental form as well as strongly associated with the ZIF-67 derived host, both in as well as outside. Further examination of four other regions in the S/H-CoS$_2$ clearly confirms that 2-5 μm pure elemental sulfur particles co-exist and remain external to the hollow host (Figure S11). Despite the fact that hollow ZIF-67 has a high void volume fraction of around 85%, a considerable amount of elemental sulfur remains outside as sulfur particles either in physical contact with or isolated from the hollow host, in a way that is similar to our previous study of a porous iron oxide.[29] S/H-CoS$_2$ together with an integrated S/Z-CoS$_2$ composite will later be compared (vide infra) in battery tests, to explore the correlation between structural design and battery performance.

We posit that the polar sulfur host obtained, CoS$_2$ in a carbon matrix derived from ZIF-67 (Z-CoS$_2$), has a strong adsorption towards polar LiPSs (lithium polysulfides). To demonstrate/test the effectiveness of Z-CoS$_2$ as a host material for suppressing the diffusion of LiPSs, the adsorption ability of polar Z-CoS$_2$ towards LiPSs was tested. ZIF-67 derived CoS$_2$ in a carbon matrix without sulfur (Z-CoS$_2$), was obtained by subliming sulfur under high temperature (300 °C) for 6 hours in a flow furnace. Z-CoS$_2$ was then mixed with a 1 mM Li$_2$S$_6$ in DOL/DME (1:1, v/v) solution as a representative polysulfide. As shown in Figure 5a, it is evident that the addition of Z-CoS$_2$ to the polysulfide solution turns the color of the Li$_2$S$_6$ from yellow to colorless (immediately), suggesting that Z-CoS$_2$ has a strong (and fast) adsorption affinity/capability for LiPSs. Thus, there would be the expectation that during cycling, Z-CoS$_2$ can help immobilize the LiPSs and greatly mitigate capacity fade. As a comparison, commercial CoS$_2$ and ZIF-67 were also added to the polysulfide solution. The commercial CoS$_2$ gave rise to a slight color change, indicating that CoS$_2$ is beneficial for constraining LiPSs, as previously reported.[35,56,72] However, ZIF-67 did not cause any discoloration. Instead the solution changed to pinkish, suggesting that ZIF-67 lacks the ability to restrain the LiPSs from diffusing and, even worse, ZIF-67 is likely decomposing slightly with Co^{2+} diffusing into the electrolyte (giving rise to the pink coloration). UV-Vis spectra (Figure 5b) further indicated that Z-CoS$_2$ has a strong entrapment ability to polysulfides, due to both chemical interactions and physical constraints. The strong and fast affinity of Z-CoS$_2$ for LiPSs could improve cycling stability of S/Z-CoS$_2$ composites.

Electrochemical performance: Coin cells with S/Z-CoS$_2$, S/ZIF-67 and S/H-CoS$_2$ as cathode materials were prepared to evaluate their electrochemical performance. Cyclic voltammograms (CV) of these materials were obtained over the voltage range of 1.7-3.0 V at a scan rate of 0.1 mV s^{-1} (Figures 6a-c). For S/Z-CoS$_2$, two well-defined reduction peaks at 2.28 and 2.05 V were observed, corresponding to the reduction of sulfur to high-order lithium polysulfides Li$_2$S$_x$ ($4 \leq x \leq 8$) as well as lithium polysulfides to solid-state Li$_2$S$_2$/Li$_2$S, respectively, while the anodic peak could be assigned to the oxidation of Li$_2$S$_2$/Li$_2$S to S$_8$. In the case of S/ZIF-67, the two reduction peaks were found at lower potentials of 2.22 V and 1.98 V, respectively. The potential shifts are likely due to the low electronic conductivity of ZIF-67, which results in slower redox kinetics. As mentioned previously, the heat treatment carbonizes the ZIF-67 material to produce CoS$_2$ in the carbon matrix. Benefitting from the generated carbon as well as CoS$_2$, the overall conductivity of the composite material is enhanced, facilitating electronic transfer. Due to the similar reaction pathways, S/H-CoS$_2$ has higher conductivity than S/ZIF-67, leading to a positive shift of the reduction peaks (2.23 and 2.01V) compared to S/ZIF-67. However, the external elemental sulfur on the surface of the host material impedes electron transfer between particles, so that the reaction kinetics are slower than for S/Z-CoS$_2$. To compare the conductivity of the materials, electrochemical impedance spectra (EIS) of S/Z-CoS$_2$, S/ZIF-67 and S/H-CoS$_2$ cathodes are presented in Figure S12. S/Z-CoS$_2$ exhibits the smallest semicircle diameter in the high-frequency region, suggesting that S/Z-CoS$_2$ has the faster charge transfer processes. In addition, Figures 6a-c show that after 10 CV cycles, the peak positions and intensities were not changed for S/Z-CoS$_2$, indicating the stable cycling stability of the material. In contrast, both S/ZIF-67 and S/H-CoS$_2$ exhibited dramatic shifts and decreased intensities, due to severe polysulfide shuttling.

The cycling performance of these three electrodes are compared at a current density of 0.2 C (Figure 6d). S/Z-CoS$_2$, S/ZIF-67 and S/H-CoS$_2$ delivered initial capacities of 993, 900, and 970 mAh g^{-1}, respectively. However, after only 50 cycles, the discharge capacity of S/ZIF-67 dropped rapidly to 300 mAh g^{-1}, corresponding to a capacity retention of only 30%. The rapid capacity decay is due to the fast polysulfide dissolution, which is in agreement with Figure 6c. The S/H-CoS$_2$ electrode delivered a somewhat higher capacity with slightly better capacity retention than S/ZIF-67 because of the increased electrical conductivity, caused by heat treatment, and chemical interactions between CoS$_2$ and LiPSs during cycling. However, with minimal chemical adsorption effects, the capacity fade was still severe with only 28% retention after 200 cycles. In contrast,

S/Z-CoS$_2$ electrodes exhibited a significantly enhanced cycling stability. A much higher capacity of 750 mAh g^{-1} was achieved with an excellent capacity retention of 76% after 200 cycles. The improved stability is likely due to the increased conductivity of the material, compared to S/ZIF-67, and mitigated loss of active material, through LiPSs dissolution, by both physical confinement and the chemical interactions of LiPSs with CoS$_2$ in the carbon matrix. The capacity values obtained based on the mass of the composite are shown in Figure S13. The prolonged cycling stability of the materials was further tested at 1 C (Figure 6e). S/Z-CoS$_2$ exhibited a highly stabilized capacity of 440 mAh g^{-1} after 1000 cycles, corresponding to a low average capacity drop rate of 0.04% per cycle.

The rate capabilities and the electrode kinetics were investigated at various current densities (Figure 7a). As the current density was increased stepwise from 0.1 to 5 C, the S/Z-CoS$_2$ delivered high capacity values of 1100, 910, 740, 640, 580, 490 and 430 mAh g^{-1}, respectively. When the current density was decreased back to 0.1 C, a capacity of 930 mAh g^{-1} was obtained, indicating a high structural stability, even at high C-rates. Compared with S/Z-CoS$_2$, the S/ZIF-67 shows much lower discharge capacities at various current densities, and almost no capacity at current densities higher than 2 C. The dramatically low capacities are caused, at least in part, by the low conductivity of the composite material (Figure S12). Owing to the higher conductivity of H-CoS$_2$, the rate capability of S/H-CoS$_2$ is better than S/ZIF-67 at high current densities. However, without efficient physical constraint, the ineffective LiPSs confinement of H-CoS$_2$ results in relatively low capacities at low C-rates. It is worth noting that S/H-CoS$_2$ and S/Z-CoS$_2$ have similarly high capacities at high current densities. This could be due to CoS$_2$, serving as an electrocatalyst, could favorably affect the redox reactions.[56,72] Ascribed to the improved conductivity and efficient LiPSs entrapment by both physical confinement and chemical adsorption effects, S/Z-CoS$_2$ exhibited the best performance in terms of redox kinetics and cycling stability.

High sulfur loading of the electrode composite is of great significance for the practical use of Li–S batteries. Thus, S/Z-CoS$_2$ electrodes with high areal sulfur loadings of 2.5-2.9 mg cm^{-2} were further tested. Figure 7c presents cycling performance of the high-loading electrodes cycled at 0.2 C for 150 cycles. An initial discharge capacity of 1030 mAh g^{-1} was achieved, corresponding to an areal capacity of 3 mAh cm^{-2}. After 150 cycles, a high and stabilized specific capacity of 750 mAh g^{-1}, corresponding to 2.2 mAh cm^{-2}, was obtained. The stable cycling performance of high-loading sulfur electrodes of S/Z-CoS$_2$ is ascribed to the high conductivity of S/Z-CoS$_2$ and efficient

confinement of LiPSs by both physical and chemical entrapment. The rate performance of high-loading electrodes in Figure 7b shows that the S/Z-CoS$_2$ electrode can provide a high areal capacity of 1.5 mAh cm^{-2} even at a high C rate of 1 C. Two well-defined discharge plateaus were observed at various current densities (Figure S14), illustrating the fast redox kinetics of the electrodes.

Furthermore, to study the reaction kinetics of the electrodes, the galvanostatic intermittent titration technique (GITT) was employed by discharging/charging the cell for 30 min at 0.1 C followed by a 10-hour rest period. The lithium ion diffusion coefficient at different states of charge (SOC), could be calculated from the transient voltage response using the expression developed by Weppner and Huggins.[73] The lithium ion diffusion coefficients calculated using this equation at different SOC are plotted in Figures S15a and b. The values are found to be higher at the first discharge plateau than those at the second plateau, confirming that the reaction of S$_8$ to Li$_2$S$_4$ is faster than the transformation of Li$_2$S$_4$ to Li$_2$S, so the liquid-solid reaction is the rate-determining step in the sulfur reduction. Moreover, CV tests at different scan rates were further conducted to study the reaction kinetics of the electrodes (Figures 8a-c). At higher sweep rates, the potentials of the reduction peaks of S/Z-CoS$_2$ are the highest while those of the oxidation peaks are the lowest among three samples of S/Z-CoS$_2$, S/ZIF-67 and S/H-CoS$_2$, further indicating that the S/Z-CoS$_2$ composites have the fastest kinetics for the reaction between Li$_2$S and S$_8$. The Li$^+$ diffusion coefficient can be derived by analyzing the CV data at different scan rates according to the Randles-Sevcik equation:

$$I_p = 2.69 \times 10^5 n^{3/2} A D^{1/2} C \upsilon^{1/2}$$

where I$_p$ is the peak current, n is the charge transfer number, A is the geometric area of the active electrode, D is the lithium ion diffusion coefficient, C is the concentration of Li$^+$, and υ is the potential scan rate. The lithium ion diffusion coefficients can be determined by plotting the current density I$_p$, versus the square root of the scan rate $\upsilon^{1/2}$ (Figure 8d-f). The linear relationship of I$_p$ versus $\upsilon^{1/2}$ indicates that the reaction is a diffusion-controlled process. For Z-CoS$_2$ encapsulating sulfur electrode, the slopes are the highest among the three samples. For peak C1 (Figure 8d), the diffusion rate increased by 29% and 34% for peak C2, respectively (Figure 8e), compared to S/ZIF-67 electrodes. These results suggest that ZIF-67 derived CoS$_2$ embedded in carbon framework could significantly enhance the redox reaction kinetics, especially for the transformation from Li$_2$S$_4$ to Li$_2$S.

All of these results indicate that S/Z-CoS$_2$ is a promising sulfur cathode material for high energy density Li–S batteries with stable cycling life and outstanding rate performance. By comparing with other cathodes based on carbon, metal sulfides/oxides or MOF materials as hosts (Table S1), it is evident that our S/Z-CoS$_2$ exhibits highly enhanced rate capability and outstanding cycling stability. The significantly improved performance is ascribed to various reasons. First, the heat treatment, which produced a carbon framework, significantly increased the conductivity of the composite (Figure S12), increasing the utilization of active material during cycling and lowering the polarization in the coin cells. Second, the polar CoS$_2$ embedded in the carbon framework can provide strong adsorption to LiPSs, enriching the LiPSs concentration on the conductive host surface, thus accelerating the redox reaction. This has been verified by the adsorption test (Figure 5). Third, *in situ* encapsulation of sulfur particles gives rise to an intimate contact between the host material and sulfur particles, and at the same time, provides a protective cage for physically restraining the LiPSs from diffusing into the electrolyte. The combined effects of physical confinement and chemical interactions give rise to the enhanced cycling stability. In addition to the physical and chemical entrapment of LiPSs, CoS$_2$ also serves as an electrocatalyst which can accelerate the polysulfides redox kinetics, especially for the liquid-solid state reaction, as manifested by the kinetic analysis (Figure 8). It is also proposed that CoS$_2$ could control the precipitation of insoluble Li$_2$S. The SEM images of a fully discharged cell after 20 cycles displayed in Figure S16 indicate that there are no bulk Li$_2$S particles present on the surface and the morphology of the composite has no noticeable changes, indicating the controlled precipitation and stable encapsulation of the active material. Recent pioneering work has also demonstrated the effectiveness of introducing a conductive interlayer to improve the cycling performance and rate capability of Li–S batteries.[40] We believe that optimizing the composite composition ratio and other components in the cell, such as introduction of an interlayer or separator modification, will likely further enhance electrochemical performance.

Conclusions

In summary, a facile and scalable method was developed to synthesize S/Z-CoS$_2$ composites via *in situ* encapsulation followed by heat treatment. The annealing process transformed ZIF-67 to CoS$_2$ embedded in a carbon framework. The formation of CoS$_2$ embedded in a carbon framework was confirmed by XAS and Cryo-TEM. The successful encapsulation of sulfur by ZIF-derived

CoS_2 in a carbon matrix was examined through Cryo-S/TEM imaging together with EDX elemental mapping. We have demonstrated that the encapsulation of sulfur particles by CoS_2 embedded in a carbon framework is beneficial for preventing/precluding the LiPSs from diffusing into the electrolyte during cycling and can also accelerate the redox reactions. Benefitting from the improved conductivity, both physical entrapment of LiPSs and their chemical binding to CoS_2, and more importantly, accelerated redox kinetics induced by CoS_2 as an electrocatalyst, the resulting S/Z-CoS_2 could achieve a high areal capacity, excellent cycling stability and enhanced rate performance. This work provides valuable insights for novel and cost-effective sulfur host materials design for the future practical application of high-energy, high-power and long-life Li–S batteries.

Author Information

Corresponding author:

*H.D.A.: hda1@cornell.edu

Author Contributions:

[#]N.Z. and Y.Y. contributed equally to this work.

N.Z. synthesized the materials, conducted the electrochemical study and wrote the manuscript. Y.Y. performed the cryogenic S/TEM imaging and EDX elemental mapping and wrote the corresponding analysis. X.F. conducted the XANES and EXAFS measurments and wrote the corresponding analysis. S.-H. Y., J.S. helped perform the experiment.

Conflicts of interest:

There are no conflicts to declare.

References

1. P. G. Bruce, S. A. Freunberger, L. J. Hardwick and J.-M. Tarascon, *Nat. Mater.*, 2011, **11**, 19–29.
2. A. Manthiram, S. H. Chung and C. Zu, *Adv. Mater.*, 2015, **27**, 1980–2006.
3. Y. Yang, G. Zheng and Y. Cui, *Chem. Soc. Rev.*, 2013, **42**, 3018–3032.
4. S.-H. Yu, X. Feng, N. Zhang, J. Seok and H. D. Abruña, *Acc. Chem. Res.*, 2018, **51**, 273–281.
5. S. Evers and L. F. Nazar, *Acc. Chem. Res.*, 2013, **46**, 1135–1143.
6. G. Zhou, S. Pei, L. Li, D. W. Wang, S. Wang, K. Huang, L. C. Yin, F. Li and H. M. Cheng, *Adv. Mater.*, 2014, **26**, 625–631.
7. J. Park, S.-H. Yu and Y.-E. Sung, *Nano Today*, 2018, **18**, 35–64.
8. S.-H. Yu, X. Huang, K. Schwarz, R. Huang, T. A. Arias, J. D. Brock and H. D. Abruña, *Energy Environ. Sci.*, 2018, **11**, 202–210.
9. Z. Deng, Z. Zhang, Y. Lai, J. Liu, J. Li and Y. Liu, *J. Electrochem. Soc.*, 2013, **160**, A553–A558.
10. J. Xu, T. Lawson, H. Fan, D. Su and G. Wang, *Adv. Energy Mater.*, 2018, **8**, 1702607.
11. X. Ji, K. T. Lee and L. F. Nazar, *Nat. Mater.*, 2009, **8**, 500–506.
12. B. Zhang, X. Qin, G. R. Li and X. P. Gao, *Energy Environ. Sci.*, 2010, **3**, 1531.
13. S. Xin, L. Gu, N. H. Zhao, Y. X. Yin, L. J. Zhou, Y. G. Guo and L. J. Wan, *J. Am. Chem. Soc.*, 2012, **134**, 18510–18513.
14. Z. Song, X. Lu, Q. Hu, J. Ren, W. Zhang, Q. Zheng and D. Lin, *J. Power Sources*, 2019, **421**, 23–31.
15. M. Ren, X. Lu, Y. Chai, X. Zhou, J. Ren, Q. Zheng and D. Lin, *J. Colloid. Interface Sci.*, 2019, **552**, 91–100.
16. Z. Yuan, H.-J. Peng, J.-Q. Huang, X.-Y. Liu, D.-W. Wang, X.-B. Cheng and Q. Zhang, *Adv. Funct. Mater.*, 2014, **24**, 6105–6112.
17. X.-B. Cheng, J.-Q. Huang, Q. Zhang, H.-J. Peng, M.-Q. Zhao and F. Wei, *Nano Energy*, 2014, **4**, 65–72.
18. Z. Wang, Y. Dong, H. Li, Z. Zhao, H. B. Wu, C. Hao, S. Liu, J. Qiu and X. W. Lou, *Nat. Commun.*, 2014, **5**, 5002.
19. L. Ji, M. Rao, H. Zheng, L. Zhang, Y. Li, W. Duan, J. Guo, E. J. Cairns and Y. Zhang, *J. Am. Chem. Soc.*, 2011, **133**, 18522–18525.
20. Y. Qiu, W. Li, W. Zhao, G. Li, Y. Hou, M. Liu, L. Zhou, F. Ye, H. Li, Z. Wei, S. Yang, W. Duan, Y. Ye, J. Guo and Y. Zhang, *Nano Lett.*, 2014, **14**, 4821–4827.
21. W. Zhou, H. Chen, Y. Yu, D. Wang, Z. Cui, F. J. Disalvo and H. D. Abruña, *ACS Nano*, 2013, **7**, 8801–8808.
22. W. Zhou, Y. Yu, H. Chen, F. J. DiSalvo and H. D. Abruña, *J. Am. Chem. Soc.*, 2013, **135**, 16736–16743.
23. J. Wang, Y. S. He and J. Yang, *Adv. Mater.*, 2015, **27**, 569–575.
24. Q. Pang, D. Kundu, M. Cuisinier and L. F. Nazar, *Nat. Commun.*, 2014, **5**, 4759.
25. X. He, H. Hou, X. Yuan, L. Huang, J. Hu, B. Liu, J. Xu, J. Xie, J. Yang, S. Liang and X. Wu, *Sci. Rep.*, 2017, **7**, 40679.
26. X. Tao, J. Wang, Z. Ying, Q. Cai, G. Zheng, Y. Gan, H. Huang, Y. Xia, C. Liang, W. Zhang and Y. Cui, *Nano Lett.*, 2014, **14**, 5288–5294.

27.   X. Liang, C. Hart, Q. Pang, A. Garsuch, T. Weiss and L. F. Nazar, *Nat. Commun.*, 2015, **6**, 5682.

28.   Y. Tao, Y. Wei, Y. Liu, J. Wang, W. Qiao, L. Ling and D. Long, *Energy Environ. Sci.*, 2016, **9**, 3230–3239.

29.   N. Zhang, B. D. A. Levin, Y. Yang, D. A. Muller and H. D. Abruña, *J. Electrochem. Soc.*, 2018, **165**, A1656–A1661.

30.   J. Ren, Y. Zhou, L. Xia, Q. Zheng, J. Liao, E. Long, F. Xie, C. Xu and D. Lin, *J. Mater. Chem. A*, 2018, **6**, 13835–13847.

31.   J. Zhang, Z. Li and X. W. D. Lou, *Angew Chem. Int. Ed. Engl.*, 2017, **56**, 14107–14112.

32.   X. Hong, S. Li, X. Tang, Z. Sun and F. Li, *J. Alloys and Compd.*, 2018, **749**, 586–593.

33.   J. Zhang, L. Yu and X. W. D. Lou, *Nano Res.*, 2017, **10**, 4298–4304.

34.   Z. Ma, Z. Li, K. Hu, D. Liu, J. Huo and S. Wang, *J. Power Sources*, 2016, **325**, 71–78.

35.   H. Zhang, Z. Zhao, Y.-N. Hou, Y. Tang, J. Liang, X. Liu, Z. Zhang, X. Wang and J. Qiu, *J. Mater. Chem. A*, 2019, **7**, 9230–9240.

36.   L.B. Ma, H. Yuan, W.J. Zhang, G.Y. Zhu, Y.R. Wang, Y. Hu, P.Y. Zhao, R.P. Chen, T. Chen, J. Liu, Z. Hu and Z. Jin, *Nano Lett.,* 2017, **17**, 7839–7846.

37.   C. Li, J. Shi, L. Zhu, Y. Zhao, J. Lu and L. Xu, *Nano Res.*, 2018, **11**, 4302–4312.

38.   X. Liang, A. Garsuch and L.F. Nazar, *Angew. Chem.,Int. Ed.,* 2015, **54**, 3907–3911.

39.   E. S. Sim, G. S. Yi, M. Je, Y. Lee and Y. C. Chung, *J. Power Sources*, 2017, **342**, 64–69.

40.   Q. Jin, N. Zhang, C. C. Zhu, H. Gao and X. T. Zhang, *Nanoscale*, 2018, **10**, 16935–16942.

41.   Z. Xiao, Z. Li, P. Li, X. Meng and R. Wang, *ACS Nano*, 2019, **13**, 3608–3617.

42.   Q. Jin, L. Li, H. R. Wang, H. Gao, C. Zhu and X. T. Zhang, *Electrochim. Acta*, 2019, **312**, 149–156.

43.   H. Pan, J. Chen, R. Cao, V. Murugesan, N. N. Rajput, K. S. Han, K. Persson, L. Estevez, M. H. Engelhard, J.-G. Zhang, K. T. Mueller, Y. Cui, Y. Shao and J. Liu, *Nat. Energy*, 2017, **2**, 813–820.

44.   J. Zheng, J. Tian, D. Wu, M. Gu, W. Xu, C. Wang, F. Gao, M. H. Engelhard, J. G. Zhang, J. Liu and J. Xiao, *Nano Lett.*, 2014, **14**, 2345–2352.

45.   R. Demir-Cakan, M. Morcrette, F. Nouar, C. Davoisne, T. Devic, D. Gonbeau, R. Dominko, C. Serre, G. Ferey and J.-M. Tarascon, *J. Am. Chem. Soc.*, 2011, **133**, 16154–16160.

46.   G. Xu, P. Nie, H. Dou, B. Ding, L. Li and X. Zhang, *Mater. Today*, 2017, **20**, 191–209.

47.   Q. Pang, X. Liang, C. Y. Kwok and L. F. Nazar, *Nat. Energy*, 2016, **1**, 16132.

48.   W. Xia, A. Mahmood, R. Zou and Q. Xu, *Energy Environ. Sci.*, 2015, **8**, 1837–1866.

49.   H. B. Wu and X. W. D. Lou, *Sci. Adv.*, 2017, **3**, eaap9252.

50.   G. Zhong, D. Liu and J. Zhang, *J. Mater. Chem. A*, 2018, **6**, 1887–1899.

51.   J. Zhou, R. Li, X. Fan, Y. Chen, R. Han, W. Li, J. Zheng, B. Wang and X. Li, *Energy Environ. Sci.*, 2014, **7**, 2715.

52.   Z. Wang, B. Wang, Y. Yang, Y. Cui, Z. Wang, B. Chen and G. Qian, *ACS Appl. Mater. Interfaces*, 2015, **7**, 20999–21004.

53.   G. Xu, B. Ding, L. Shen, P. Nie, J. Han and X. Zhang, *J. Mater. Chem. A*, 2013, **1**, 4490.

54.   Z. Li and L. Yin, *ACS Appl. Mater. Interfaces*, 2015, **7**, 4029–4038.

55.   J. Zhang, H. Hu, Z. Li and X.W.D. Lou, *Angew. Chem. Int. Ed.*, 2016, **55**, 3982–3986.

56.   Z. Yuan, H. J. Peng, T. Z. Hou, J. Q. Huang, C. M. Chen, D. W. Wang, X. B. Cheng, F. Wei and Q. Zhang, *Nano Lett.*, 2016, **16**, 519–527.

57.   Z. Jiang, Z. Li, Z. Qin, H. Sun, X. Jiao and D. Chen, *Nanoscale*, 2013, **5**, 11770–11775.

58.   H. Hu, B. Guan, B. Xia and X.W.D. Lou, *J. Am. Chem. Soc.*, 2015, **137**, 5590–5595.

59.	M. Hu, Y. Ju, K. Liang, T. Suma, J. Cui and F. Caruso, *Adv. Funct. Mater.*, 2016, **26**, 5827–5834.
60.	B. Ravel and M. Newville, *J. Synchrotron Radiat*, 2005, **12**, 537–541.
61.	D. B. Nash, *Icarus*, 1987, **72**, 1–34.
62.	A. G. M. Ferreira and L. Q. Lobo, *J. Chem. Thermodyn.*, 2011, **43**, 95–104.
63.	C. Raiß, K. Peppler, J. Janek and P. Adelhelm, *Carbon*, 2014, **79**, 245–255.
64.	X. Liu, J. Q. Huang, Q. Zhang and L. Mai, *Adv. Mater.*, 2017, **29,** 1601759.
65.	Q. Fan, W. Liu, Z. Weng, Y. Sun and H. Wang, *J. Am. Chem. Soc.*, 2015, **137**, 12946–12953.
66.	B. D. A. Levin, M. J. Zachman, J. G. Werner, R. Sahore, K. X. Nguyen, Y. Han, B. Xie, L. Ma, L. A. Archer, E. P. Giannelis, U. Wiesner, L. F. Kourkoutis and D. A. Muller, *Microsc. Microanal.*, 2017, **23**, 155–162.
67.	R. Sahore, B. D. A. Levin, M. Pan, D. A. Muller, F. J. DiSalvo and E. P. Giannelis, *Adv. Energy Mater.*, 2016, **6**, 1600134.
68.	X.-C. Liu, Y. Yang, J. Wu, M. Liu, S. P. Zhou, B. D. A. Levin, X.-D. Zhou, H. Cong, D. A. Muller, P. M. Ajayan, H. D. Abruña and F.-S. Ke, *ACS Energy Lett.*, 2018, **3**, 1325–1330.
69.	S. Wu, Y. Wang, S. Na, C. Chen, T. Yu, H. Wang and H. Zang, *J. Mater. Chem. A*, 2017, **5**, 17352–17359.
70.	J. Zhou, N. Lin, W. L. Cai, C. Guo, K. Zhang, J. B. Zhou, Y. Zhu and Y. Qian, *Electrochim. Acta*, 2016, **218**, 243–251.
71.	J. Xu, W. Zhang, Y. Chen, H. Fan, D. Su and G. Wang, *J. Mater. Chem. A*, 2018, **6**, 2797–2807.
72.	G. Zhou, H. Tian, Y. Jin, X. Tao, B. Liu, R. Zhang, Z. W. Seh, D. Zhuo, Y. Liu, J. Sun, J. Zhao, C. Zu, D. S. Wu, Q. Zhang and Y. Cui, *Proc. Natl. Acad. Sci. USA*, 2017, **114**, 840–845.
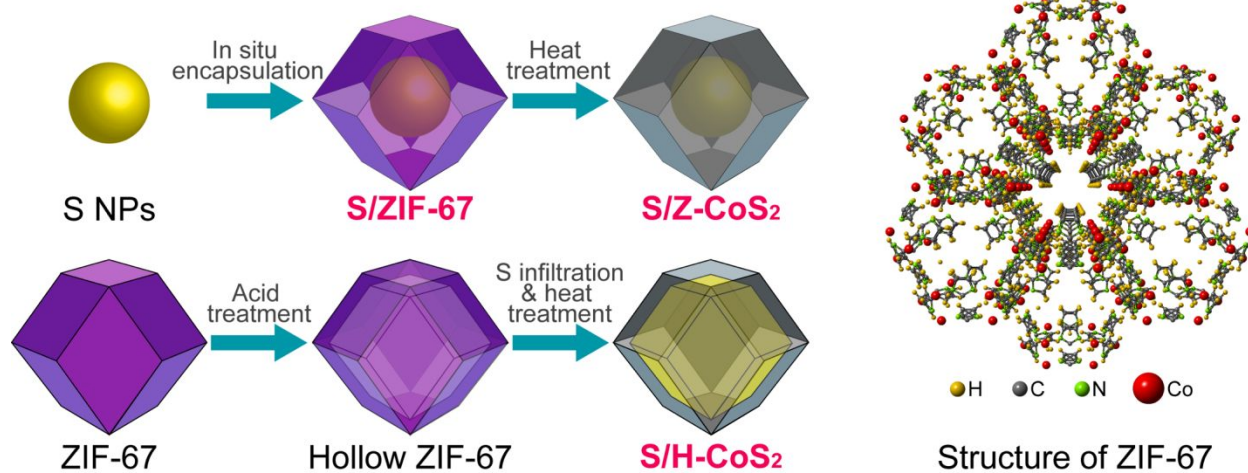73.	W. Weppner, *J. Electrochem. Soc.*, 1977, **124**, 1569.

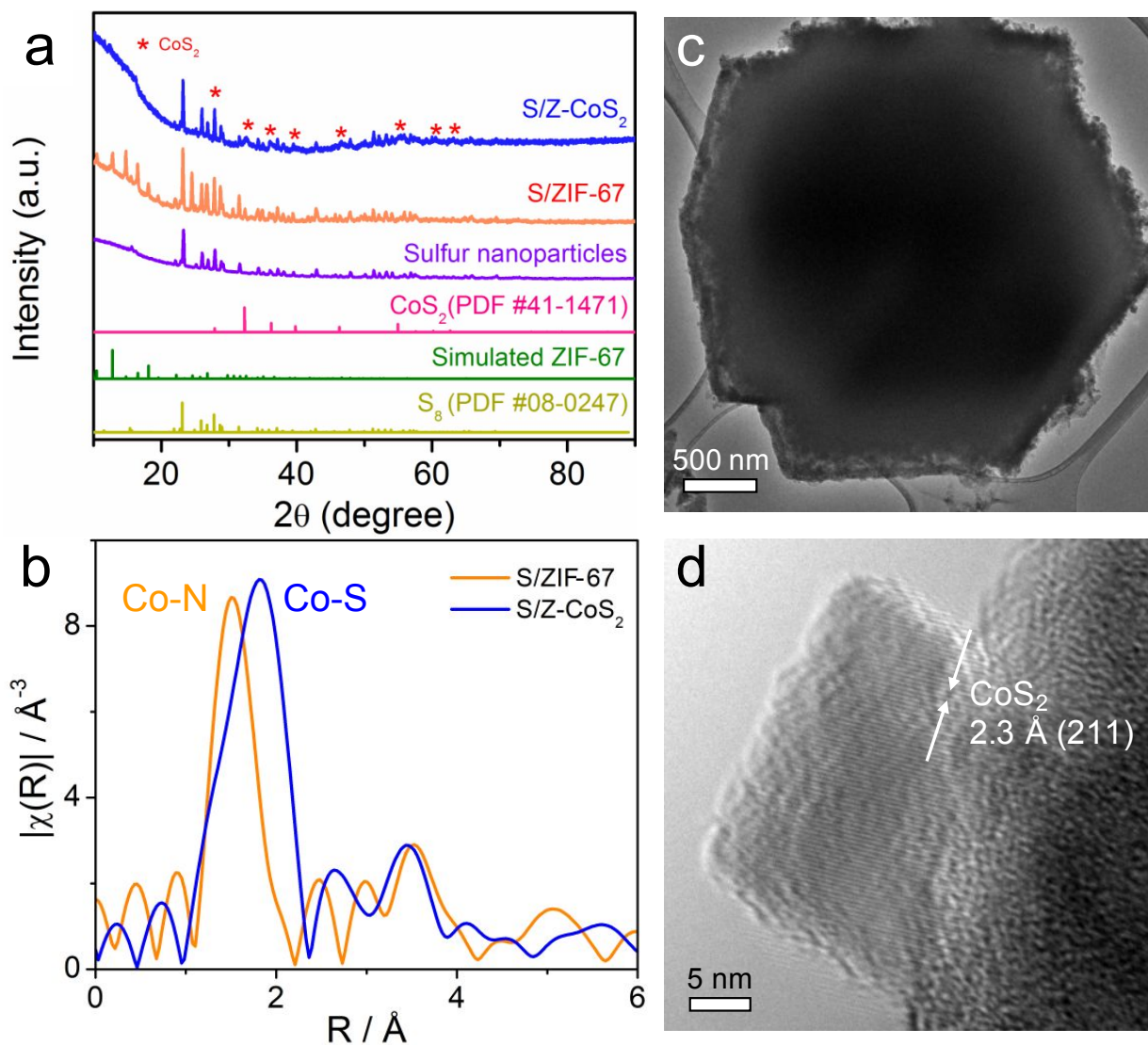**Figure 1**. Schematic illustration of the synthesis procedures of S/ZIF-67, S/Z-CoS$_2$ and S/H-CoS$_2$.

Figure 2. (a) Powder XRD patterns of sulfur/ZIF-67 composite (S/ZIF-67), sulfur/ZIF-67-derived CoS_2 in a carbon framework (S/Z-CoS_2) and as-synthesized sulfur nanoparticles and standard XRD patterns of CoS_2, ZIF-67 and elemental S_8. (b) EXAFS spectra of S/ZIF-67 and S/Z-CoS_2 with k^2-weighting and no phase correction. EXAFS fitting results and XANES spectra can be found in Figures S2-S3. (c) Cryogenic Bright-field (BF) TEM images of S/Z-CoS_2 showing the projected hexagonal symmetry and the rough surface at T= -183 ºC. (d) Atomic-scale BF-TEM image of a CoS_2 nanoparticle.
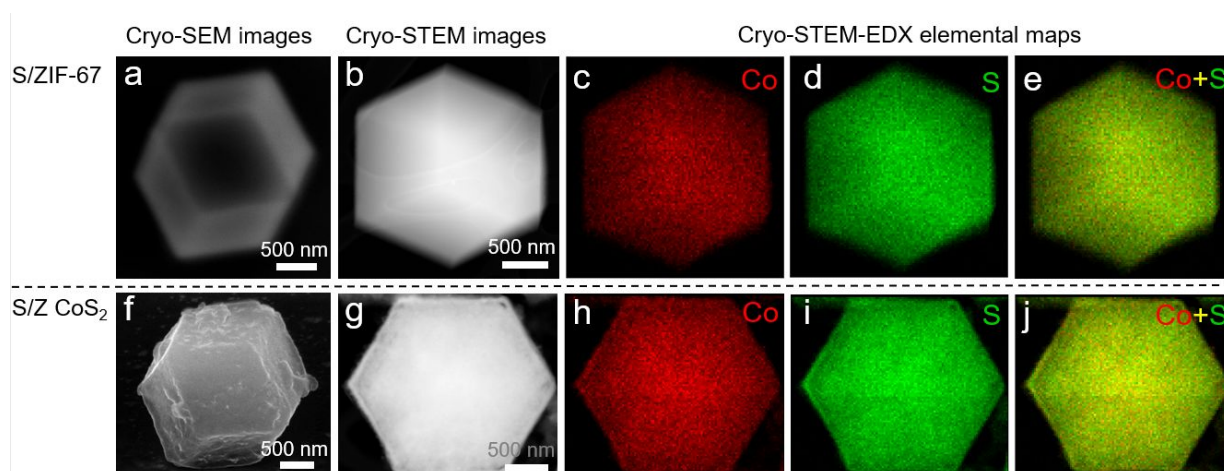
Figure 3. Cryogenic Electron microscopy (Cryo-EM) imaging and EDX elemental mapping. (a) Cryo-SEM image of S/ZIF-67 composite at T = -165 ºC. (b) Cryo-STEM image of S/ZIF-67 at T = -183 ºC. (c-e) STEM-EDX elemental maps of Co (red), S (green) and color overlay (yellow) of and Co and S, corresponding to the particle in (b). (f) Cryo-SEM image of S/Z-CoS$_2$. (g) Cryo-STEM image of S/Z-CoS$_2$. (h-j) Cryo-STEM-EDX elemental maps of Co (red), S (green) and color overlay (yellow) of and Co and S, corresponding to the particle in (g). EDX spectrum corresponding to the particle in (g) can be found in Figure S9. More examples of EDX maps of S/ZIF-67 and S/Z-CoS$_2$ can be found in Figures S6 and S8, respectively.
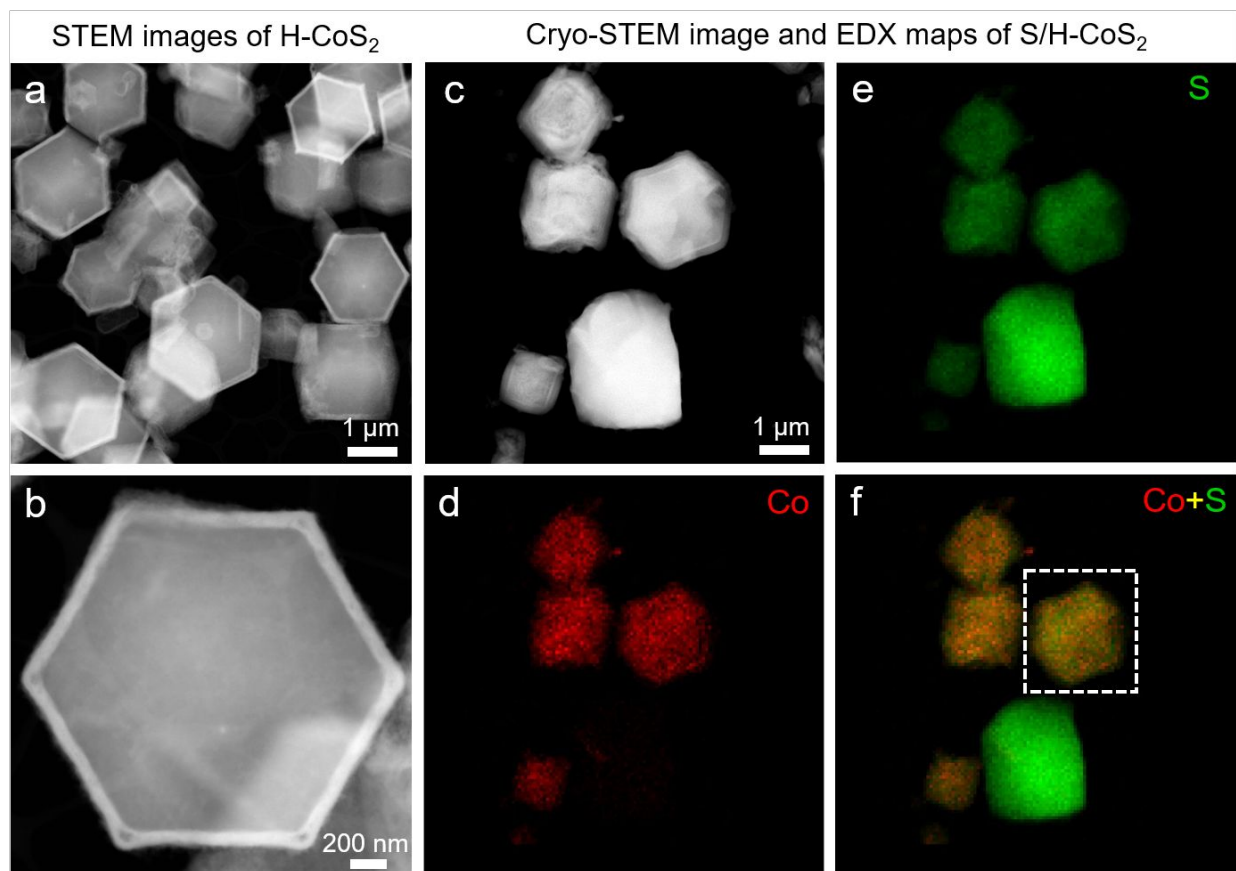
Figure 4. (a) HAADF-STEM image of hollow ZIF-67 micrometer-sized particles. (b) STEM image of a specific hollow ZIF-67 particle. Lower image contrast in the middle of the particles clearly suggests a hollow structure. (c) Cryo-STEM image of S/H-CoS$_2$ composite particles. (e-f) Cryo-STEM-EDX elemental maps of Co (red), S (yellow) and color overlay of Co and S. Yellow suggests an overlay of Co and S elements while green indicates pure elemental sulfur. EDX spectrum of the composite particle in the dashed box can be found in Figure S10. More examples of EDX maps of S/H-CoS$_2$ can be found in Figure S11.
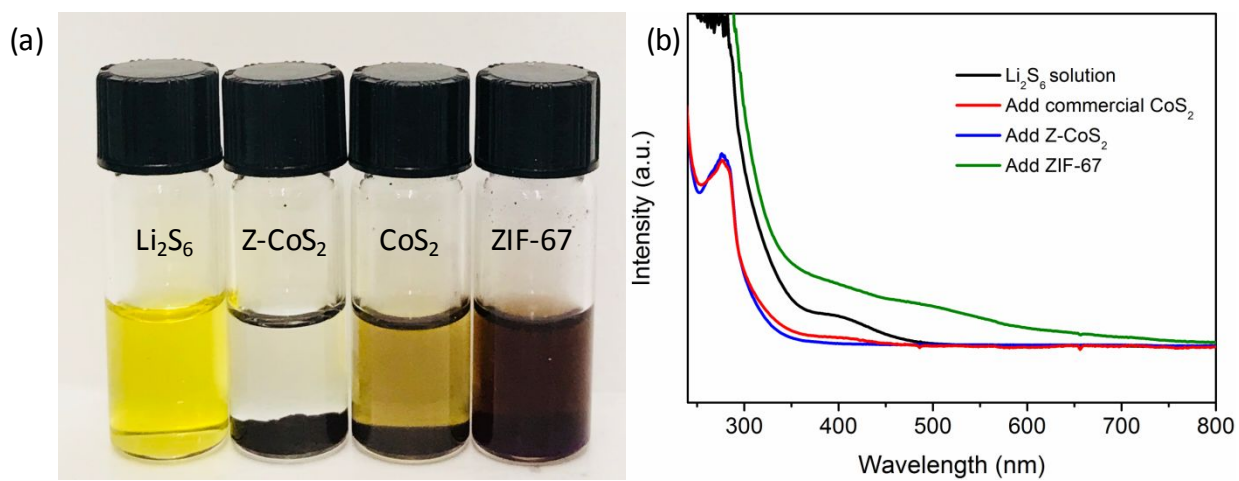
Figure 5. (a) Photographs of Li_2S_6 solution and Li_2S_6 solutions after adding Z-CoS$_2$, commercial CoS$_2$ and ZIF-67 powders. (b) UV/Vis absorption spectra of lithium polysulfide (Li_2S_6) solution before and after adding Z-CoS$_2$, commercial CoS$_2$ and ZIF-67.
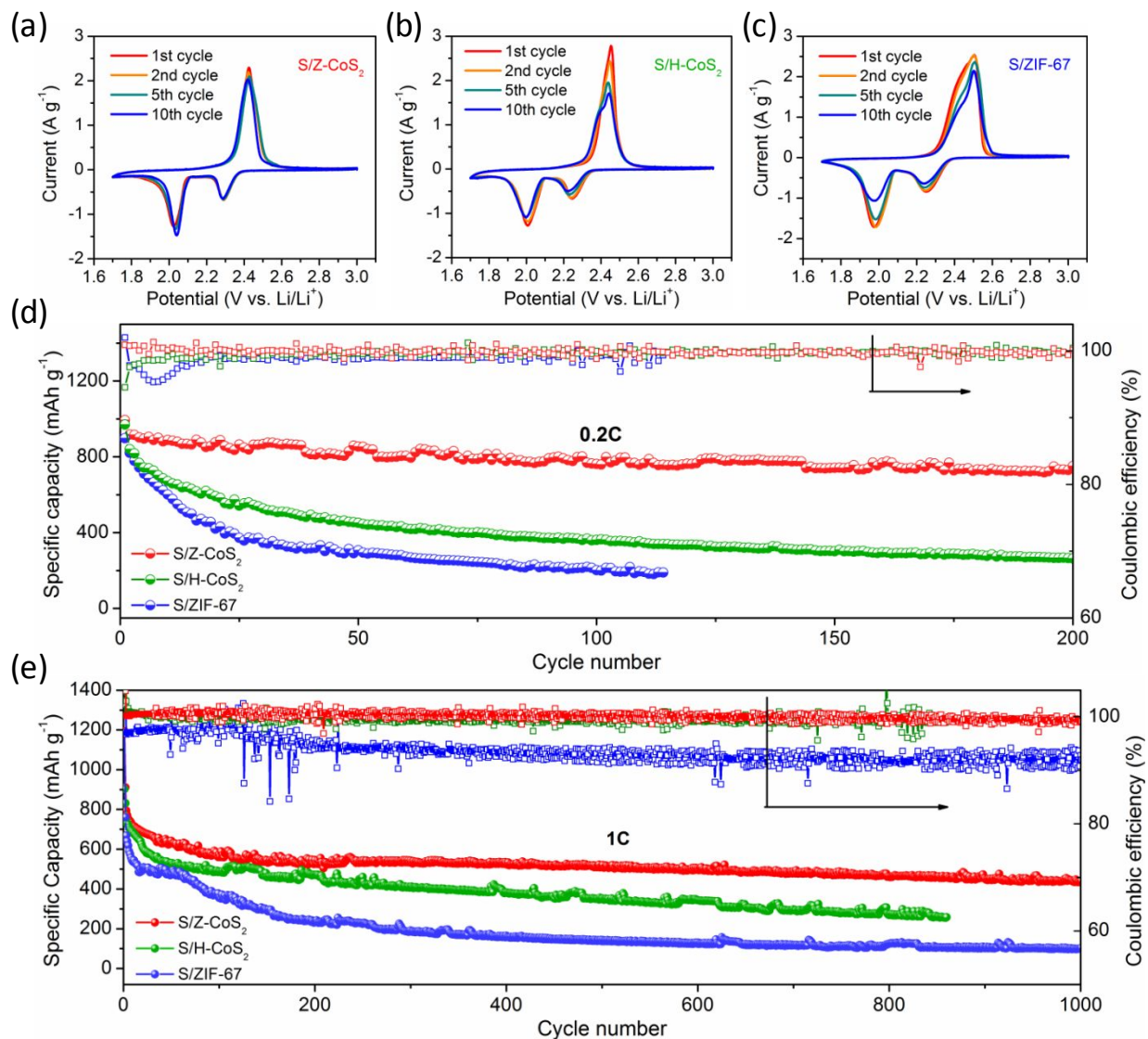
Figure 6. CV profiles of (a) S/Z-CoS$_2$, (b) S/H-CoS$_2$, and (c) S/ZIF-67 for 10 cycles at a scan rate of 0.1 mV s^{-1}. (d) Cycling performance of S/Z-CoS$_2$, S/H-CoS$_2$, and S/ZIF-67 at 0.2 C for 200 cycles. (e) Long-term cycling of S/Z-CoS$_2$, S/H-CoS$_2$, and S/ZIF-67 at 1 C for 1000 cycles.
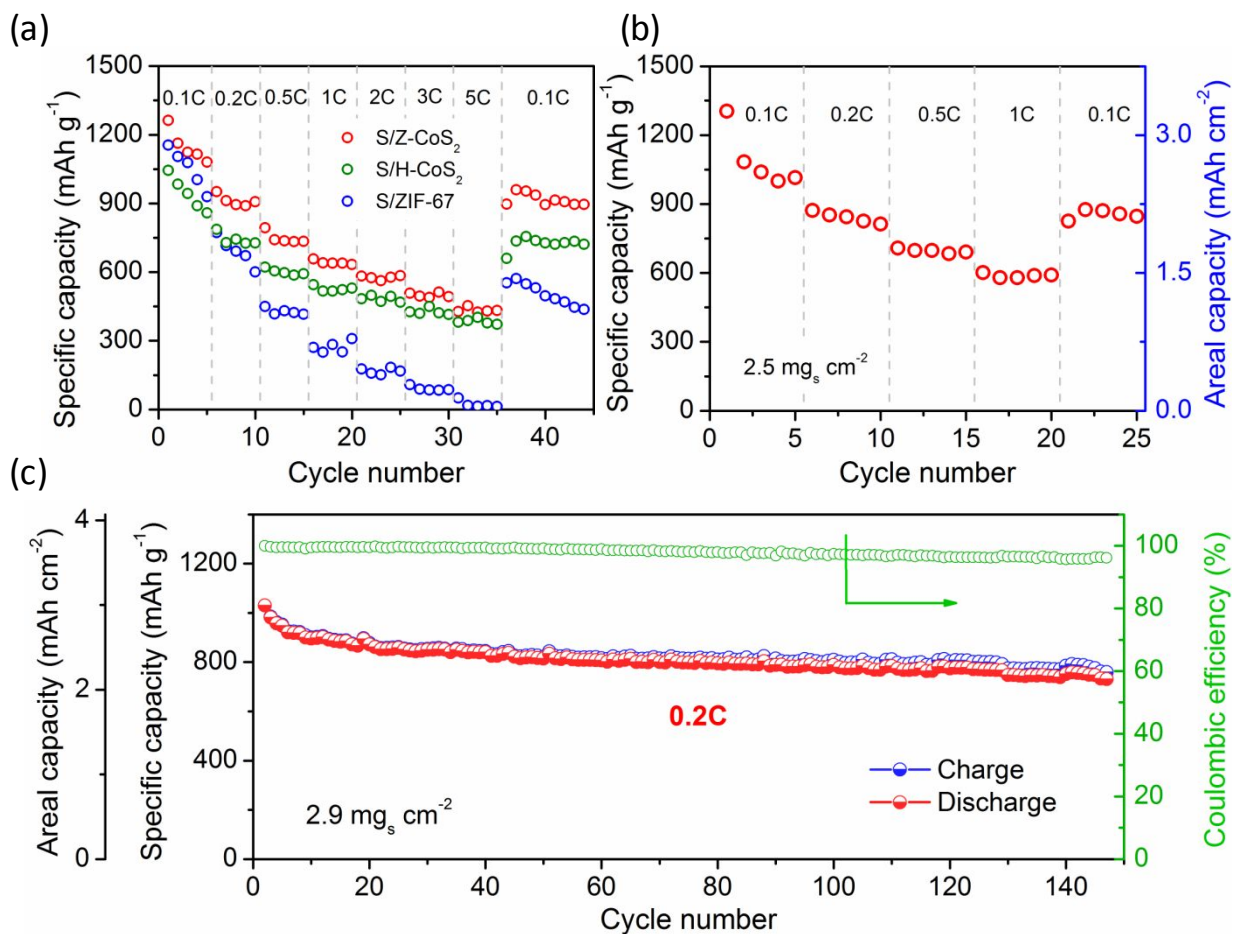
Figure 7. (a) Rate performance of S/Z-CoS$_2$, S/H-CoS$_2$, and S/ZIF-67 at C rates from 0.1 C to 5.0 C. (b) Rate performance of high sulfur loading electrodes of S/Z-CoS$_2$. (c) Cycling performance of S/Z-CoS$_2$ with high sulfur loading at 0.2 C rate.
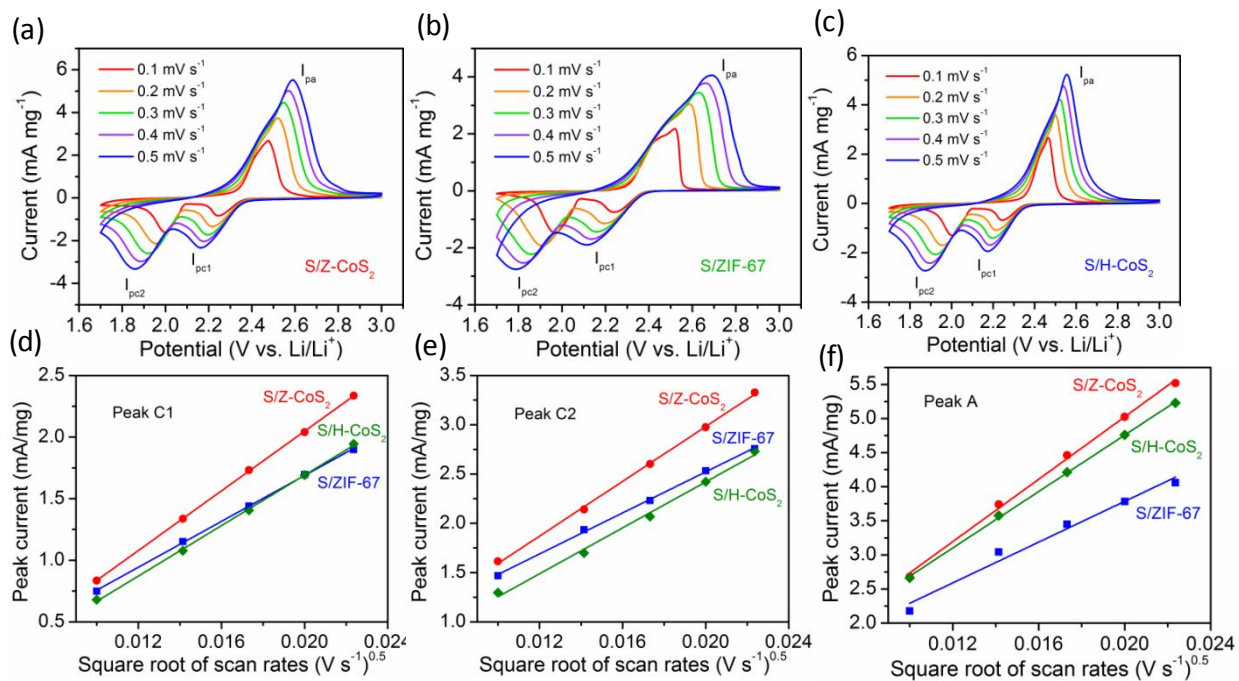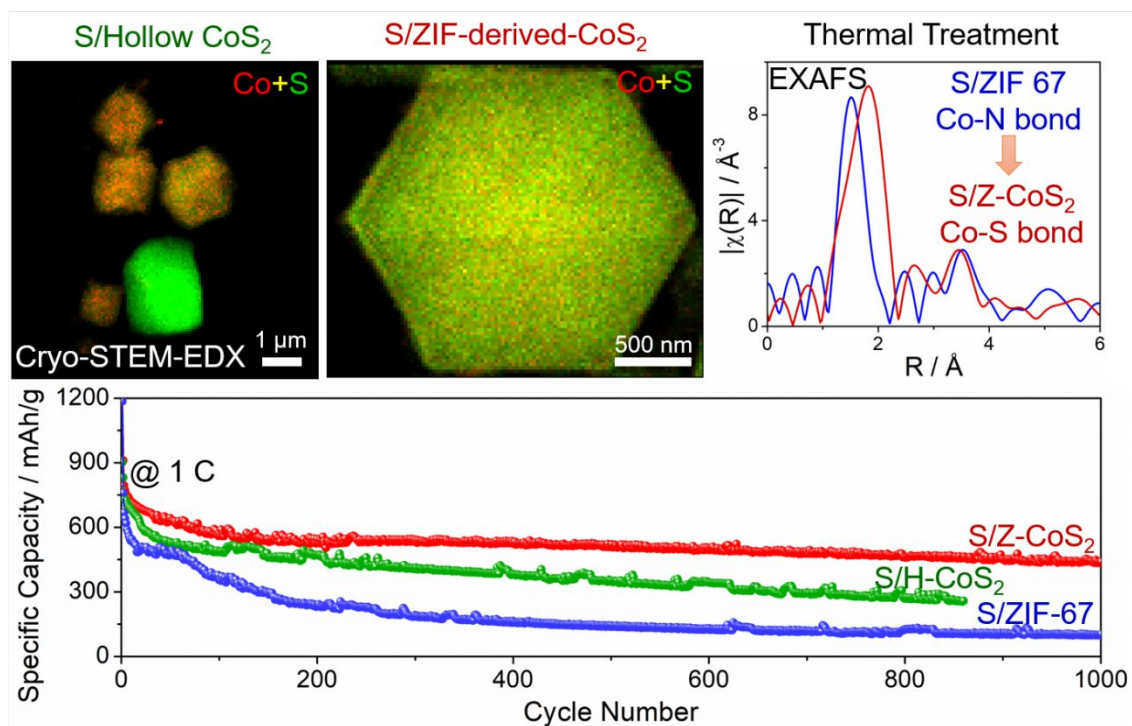
Figure 8. CV profiles of (a) S/Z-CoS$_2$, (b) S/H-CoS$_2$, and (c) S/ZIF-67 at various scan rates from 0.1 mV s^{-1} to 0.5 mV s^{-1}. Plots of S/Z-CoS$_2$, S/H-CoS$_2$, and S/ZIF-67 peak current vs square root of scan rates for (d) cathodic peak 1, (e) cathodic peak 2, and (f) anodic peak 1.

Table of Contents

The superior performance of S/ZIF-derived CoS_2 embedded in carbon framework originates from both physical confinement of sulfur inside the host and strong chemical interactions.